Microstructure and strength modelling of Al–Cu–Mg alloys during non-isothermal treatments
Part 2 – Welds

I. N. Khan, M. J. Starink*, I. Sinclair and S. C. Wang

The present work applies a model for microstructural evolution in the solid state and Al–Cu–Mg alloys and expands it in a computationally efficient way to include solid–liquid reactions in fusion welds. The model is used to predict local strength and hardness of the welds, using a formulation that incorporates hardening due to two types of precipitates, i.e. Cu–Mg co-clusters and the S phase precipitates. The model predictions are compared with hardness, differential scanning calorimetry and transmission electron microscopy data for a fusion welded 2024-T351 aluminium alloy. The model predicts solid state reactions and solid–liquid reactions including co-cluster dissolution, S phase formation, growth, coarsening and dissolution, co-cluster reformation on cooling, and solute partitioning on resolidification. The model predictions are in good agreement with the experimental results and illustrate the dominant role that (sub-)nanoscale co-clusters play in strengthening of welds. The yield strength of as welded material tested normal to the weld is mainly due to the co-clusters.

Keywords: Aluminium alloys, Ageing, Modelling, Welding, Co-clusters

Introduction

Al–Cu–Mg precipitation strengthened alloys are used in structural elements such as fuselage and lower wing surfaces in commercial airplanes.[1–7] In recent years, welding is being considered as a potential weight and cost saving alternative to riveting[3,8–10] typically in the production of the aircraft fuselage. The variable polarity plasma arc welding (VPPAW) process is widely used for welding of aluminium alloys in a range of aerospace and automotive applications.[11–13] The VPPAW process has certain similarities to the gas tungsten arc welding and yet with advantages such as high quality welds, high welding speeds and better weld penetration enabling welding of thicker plates in single pass due to higher temperature and concentrated plasma arc.[14,15]

In the companion paper,[16] a model for hardening of Al–Cu–Mg alloys was derived based on a two precipitate (S phase and co-clusters), two mechanism approach, and this model was applied to the hardening in 2024-T351 aluminium alloys during controlled heating and cooling. In the model, the evolution of the S phase was treated using the Kampmann and Wagner numerical (KW) model. The aim of the present work is to extend the same model formulation for the prediction of changes in microstructure, yield strength and hardness

in 2024-T351 aluminium alloys during a fusion welding process. An important aspect of the present work is to quantify the contribution of co-clusters in the strengthening of the welds. To this end, the authors will perform a detailed analysis of differential scanning calorimetry (DSC) measurements of the amounts of co-clusters formed, and compare that with the model predictions.

In the modelling strategy applied, the authors attempt to make appropriate approximations to arrive at a model formulation which is not computationally demanding. This is carried out both in order to clearly reveal the underlying mechanisms, as well as to allow for future application in software in conjunction with computationally demanding elements such as three-dimensional finite element heat flow predictions and thermodynamic predictions using the calculation of phase diagrams (CALPHAD) methodology (e.g. Ref. 17).

Model

In the present work, the authors are using the solid state reaction and strengthening model presented in the companion paper[16] and extend that to deal with the partial and full melting followed by solidification that occurs in and near the fusion zone.

Solid state reactions

In the solid state, a simplified precipitation reaction consistent with the two stage hardening observed in these alloys[16,18] is used in the model

Materials Research Group, School of Engineering Sciences, University of Southampton, Southampton SO17 1BJ, UK

*Corresponding author, email m.j.starink@soton.ac.uk

$$\alpha_{ss} \rightarrow Cu-Mg \text{ co clusters} \rightarrow S \text{ phase precipitates}$$

The model includes hardening contributions due to shearable co-clusters and non-shearable S phase precipitates and discussed in detail in the companion paper.[16]

Solid–liquid reactions

In the fusion welded materials, there are three distinct regions: the fusion zone, heat affected zone (HAZ) and the base metal.[19,20] The maximum temperature attained during welding is in the fusion zone, which undergoes melting and solidification. The high thermal gradients and cooling rates during welding result in non-equilibrium solidification.[20] Here, a realistic treatment of segregation during solidification of the fusion zone in a 2024 weld is achieved by considering a simplified, pseudobinary solidification formulation (single solid and liquid phase) and following the Scheil approach. The Scheil approach[21] to solidification is based on the following assumptions: the interfaces are in equilibrium; there is no diffusion in the solid phase; a homogeneous composition within the liquid phase; and equal solid and liquid phase densities.

Assuming the solidus to be approximated as a straight line, the Cu concentration in the Al rich phase solidified from the fully molten state in the fusion zone may be evaluated by[22]

$$x_{Cu}(T) = x_{Cu,g} \frac{T_m - T}{T_m - T_{sol}(x_{Cu,g})} \qquad (1)$$

where $x_{Cu,g}$ is the Cu content of the alloy, T_m is the melting temperature of pure Al, and $T_{sol}(x_{Cu,g})$ is the equilibrium solidus temperature of the alloy in the pseudobinary approximation.

Partial melting occurs when the alloy is heated between the solidus and the liquidus temperatures. Within this temperature range, the authors assume that $x_{Cu,g}$ increases linearly with temperature between the value for the material that remains fully solid and the materials that solidifies after full melting. In the zone where partial melting occurs ($T_{sol} < T < T_{liq}$), $x_{Cu,sol}$ is evaluated by

$$x_{Cu,sol} = x_{Cu,g} \frac{T_m - \{[T_{max} + T_{sol}(x_{Cu,g})]/2\}}{T_m - T_{sol}(x_{Cu,g})} \qquad (2)$$

where T_{max} is the maximum temperature achieved during partial melting.

In the fully melted region ($T > T_{liq}$), $x_{Cu,sol}$ is calculated by substituting the average temperature of the solidification range experienced by the sample, i.e. $T = (T_{liq} + T_{sol})/2$

$$x_{Cu,sol} = x_{Cu,g} \frac{T_m - \{[T_{liq}(x_{Cu,g}) + T_{sol}(x_{Cu,g})]/2\}}{T_m - T_{sol}(x_{Cu,g})} \qquad (3)$$

where $T_{liq}(x_{Cu,g})$ is the liquidus temperature of the alloy.

The simplified solution based on the pseudobinary approximation method used here ignores aspects of the real solidification path that will be more computationally demanding in modelling, e.g. other eutectic phases in the 2024 alloy such as $\theta(Al_2Cu)$, $Al_7Cu_2(Fe,Mn)$ and Al–Si–Mn–Fe phases are omitted. However, as shown later, the present pseudobinary simplification in the

model does not significantly impair accuracy of yield strength and hardness predictions.

Thermal profile

A basic requirement for prediction of microstructural and hardening changes during fusion welding is the modelling of the weld thermal profile for different regions in the material with reference to the weld centre. In the present work, the determination of the thermal profile during fusion welding is based on the Rosenthal's analytical solution for heat flow in thin plates.[22,23] The approach is based on the assumption of heat flow occurring in two dimensions, parallel to the plate surface, neglecting any heat transfer from the surface (no heat is lost by convection or radiation from the boundaries such that the heat flow perpendicular to the plate is zero). Considering a two dimensional heat flow for full penetration welds, the rise in temperature at a given point and time is then given by[23–25]

$$T - T_o = \frac{q}{2\pi K_T} \exp\left(\frac{v_h}{2\kappa}\right) K_o \left[\frac{v_h}{2\kappa}\left(x^2 + y^2\right)^{1/2}\right] \qquad (4)$$

where q is the heat input per unit time, T_o is the initial temperature of the plate, v_h is the speed of movement of the heat source, K_T is the thermal conductivity, κ is the thermal diffusivity, ρ is the density and K_o is the modified Bessel function of the second kind of order zero evaluated using a series expansion.[23] The authors use a value for κ that is appropriate for a 2024 alloys: $\kappa = 0.6078 \times 10^{-4}$ m^2 s^{-1}.[26] The value of the heat input q, which cannot be measured accurately, is selected such that the peak in hardness position immediately beside the weld coincides with the predicted position of maximum hardness.

Microstructure–strength–hardness predictions

The precipitation strengthening by the shearable Cu:Mg co-clusters is modelled on the basis of the modulus strengthening mechanism and the strengthening by the non-shearable S phase precipitates is based on the Orowan looping mechanism. Also included are the solid solution and dislocation strengthening (due to 2% stretching for T351 treatment), and total critical resolved shear stress of grains is obtained via an appropriate superposition rule.[16] Grain boundary strengthening is neglected as the grain size is too large for a significant contribution. The hardness is predicted from yield strength using a non-linear relationship. The full model is outlined in the companion paper.[16]

Experimental

The starting material was a 13 mm thick 2024-T351 alloy plate, where T351 stands for solution treated, cold stretched ($\sim2\%$) and subsequently aged at room temperature. The composition of the alloy was 4·2 wt-%Cu, 1·5 wt-%Mg, 0·6 wt-%Mn, <0·5 wt-%Si and <0·5 wt-%Fe with balance Al. Welding was performed at a travel speed of 17 cm min^{-1} in the vertical-up position. The details of the welding are presented elsewhere.[27] A full set of experiments was performed on an autogenous weld (without filler) and for a weld with additional filler (in the form of a 2319 Al–Cu based alloy), only hardness tests were performed. The surface of the welded plate was removed to a depth of ~2 mm and then mechanically polished.
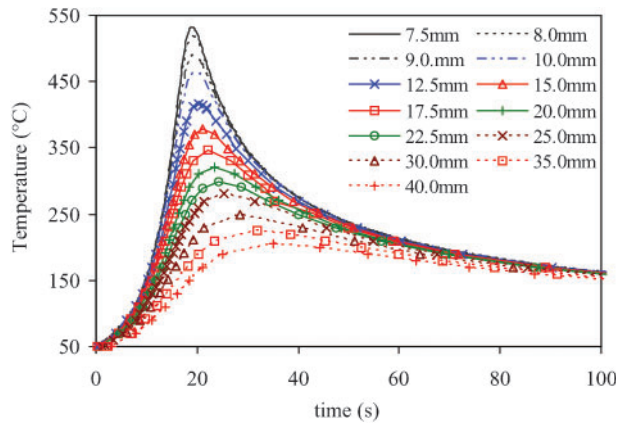
1 Thermal profile determined using Rosenthal thin plate solution for two-dimensional heat flow in plate

2 Model predictions of hardness of samples during non-isothermal representing heating rates depicted in Fig 1: experimental data from Ref. 28

Microhardness measurements were made at a load of 1 kg. Transmission electron microscopy (TEM) samples were prepared by cutting 0·4 mm thick slices at a distance of ~12·5 and ~22·5 mm from the centre of the weld and grinding to a thickness of ~0·15 mm and punching 3 mm diameter discs. The samples were polished in a twin jet electropolisher using a 30%HNO$_3$ solution in methanol maintained between −20 and −30°C. Digital dark field TEM images for the two regions were used to measure the precipitate size distribution using the dimensioning feature in AutoCAD software. Details of the experimental procedures for DSC are described in the companion paper.[16]

Results and analysis

The thermal profile during arc welding typically consists of heating very rapidly to a peak temperature which is followed by fast cooling to room temperature.[19] The heating and cooling rates during welding critically influence the microstructural changes and the mechanical properties in the weld and the HAZ.[9,22] In order to model the microstructural and strengthening changes during welding, the thermal profile $T(\vec{r},t)$ needs to be predicted. In the present work, the thermal profile prediction is based on the two-dimensional heat flow approximation (equation (4)). In Fig. 1, a plot of T as a function of time represents the predicted thermal profiles during welding at different distances from the weld centreline.

Similar to other models relying on the KW model, in the present model for solid state reactions, the interfacial energy at the precipitate matrix interface for the S phase precipitates was considered a fitting parameter in the companion paper[16] and a preceding paper.[28] In these papers, it was shown that the following expression for the interfacial energy yielded good model results

$$\gamma_n = \gamma_{n,0} - aT^3$$

where γ_n is the interfacial energy during nucleation (J m^{-2}), T is the absolute temperature, and a is a fitting parameter. In the present paper, the authors will use values that were determined in the previous papers: as in Refs. 16 and 28, a is taken as $2 \cdot 186 \times 10^{-10}$ J m^{-2} K^{-3} and $\gamma_{n,0}$ is taken as intermediate between values obtained previously through fitting the model to isothermal ageing data (0·1206 J m^{-2})[28] and through
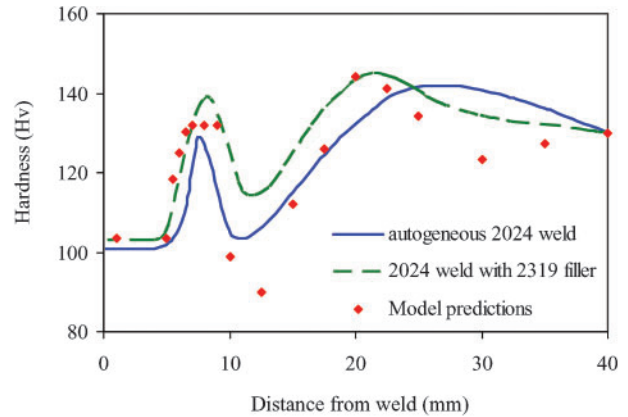
fitting the model to controlled heating and cooling data (0·1238 J m^{-2}),[16] i.e. $\gamma_{n,0}=0 \cdot 1222$ J m^{-2}.

Figure 2 presents experimental results and model predictions for hardness as a function of the distance from the weld centre. There is a good agreement in the general trends of the predicted and experimentally measured results. Both the heating and cooling cycles during welding rates affect the microstructural evolution of the S phase precipitates and in turn influence the hardness. The evolution of S phase precipitate size and volume fraction during the fusion welding and the resultant hardness changes as a function of position with respect to the weld line are presented in Fig. 3.

The key to verifying model accuracy is to independently verify the predictions for the parameters that have the strongest influence on the strength of the welded material: the amount of co-clusters and the amount and size of S phase. All three aspects are addressed. The best way to unambiguously determine precipitate size is through direct imaging, and in the present work, the authors have measured S phase sizes from TEM images. Micrographs (TEM) obtained from samples cut at a distance of 12·5 and 22·5 mm from the weld centre are presented in Fig. 4. In Fig. 5, the predicted and measured sizes of the S phase precipitates are presented. The predicted average diameters of the S phase precipitates are in agreement with the measured sizes. The measured data is listed in Table 1 (Standard error in the mean is calculated by dividing the standard deviation by the square root of the number of precipitates measured).

The DSC scans on samples cut from specific welded plate regions in Fig. 6a show heat effects which have been identified in previous work through TEM and three-dimensional atom probe studies.[16,18,29,30] The main exothermic heat effect situated between about 230 and 310°C is due to the formation of two variants of the S phase.[18] The relative amounts of the two variants of this phase depends on the amount of dislocations, nuclei and the amount of solute present (*see* the section on 'Discussion'). From its start at ~160°C to ~210°C, the endothermic effect is effectively identical to that observed in samples solution treated and aged at room temperature. The latter samples were found to contain only Cu–Mg co-clusters, and hence the DSC observations evidence the dissolution of these co-clusters.
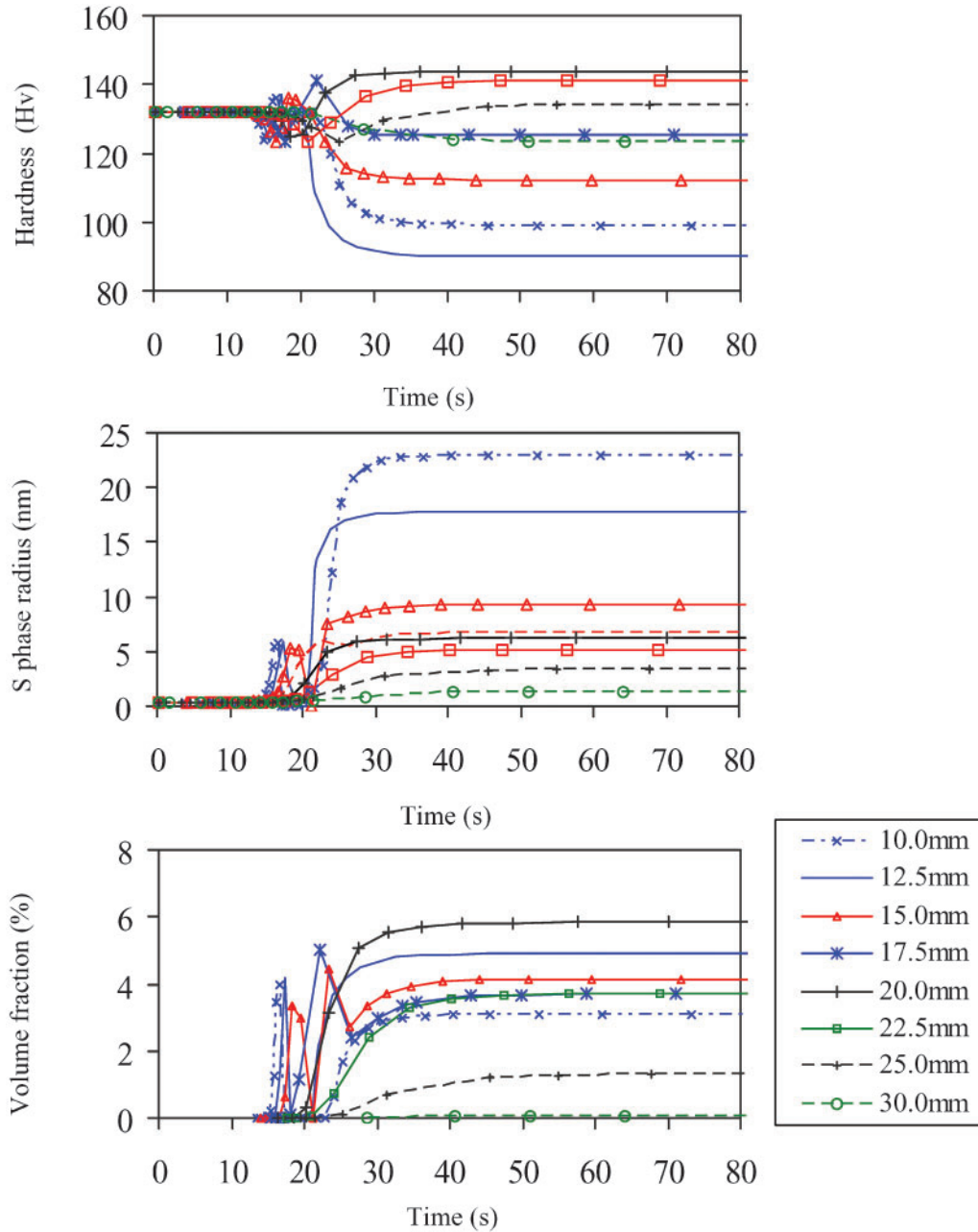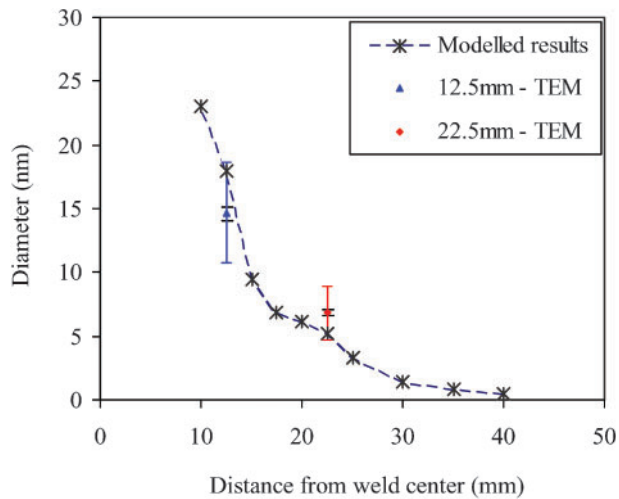
3 Evolution of S phase precipitate size and volume fraction and resultant hardness changes in different regions (determined as distances from weld centre) during fusion welding
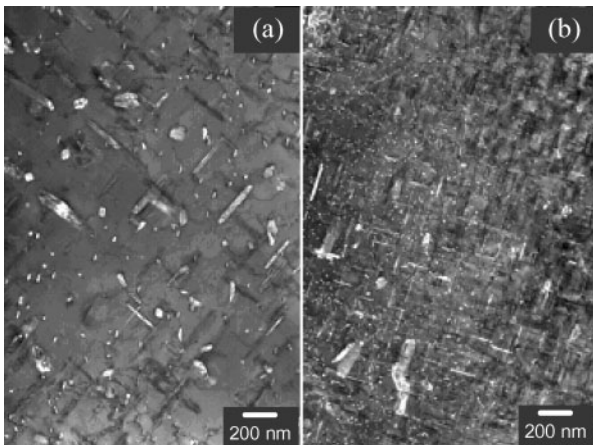
4 TEM dark field images for *a* position 4 (12·5 mm from centreline) and *b* position 5 (22·5 mm from centreline)

Beyond 210°C, the endothermic heat effects diverge due to overlap with the S phase formation effect, which depends (both in terms of start temperature as well as heat content) on the position in the sample.

The authors compared the predicted changes in the fraction of Cu–Mg co-clusters transformed during the welding with data obtained from the DCS scans in Fig. 6*a*. A comparison of the predicted and measured volume fractions of Cu–Mg co-clusters is presented in Fig. 6*b*. The results have been normalized by dividing by the maximum predicted and measured volume fraction respectively. The general trends for both the model predictions and the experimental results are in good agreement. Also the trends for the amount of S phase precipitation (the main exothermic effect in the DSC curves in Fig. 6*a*) follow closely the amounts of solute predicted to be available for precipitation, and hence the

5 **Modelled average size of S phase precipitates compared with average size measured from TEM images (Fig. 4) obtained from samples cut at 12·5 and 22·5 mm from weld centre: larger error bars represent standard deviation of sample and smaller error bars represent accuracy in determination of mean**

model also predicts the amount of S phase formed during welding well.

Further microstructural data on the welds obtained by TEM and scanning electron microscopy have been published elsewhere.[22] Also this additional data are broadly in agreement with the present model. One exception is that the detailed TEM work shows the presence of limited amounts of additional precipitate and eutectic phases, Ω and θ.
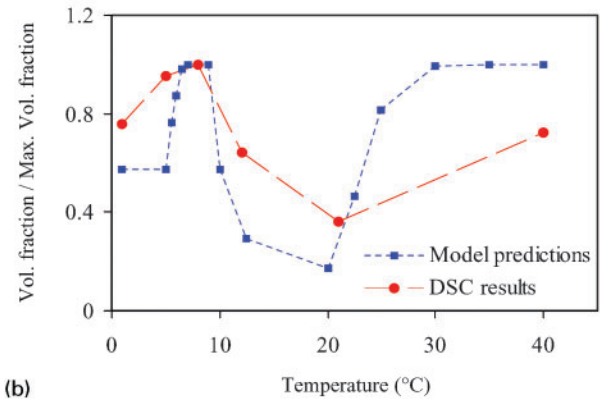
Discussion

Model parameters and approximations in KW model

The present publication provides the first work in which a two stage–two mechanism model for strengthening in an alloy is used to predict local microstructure and strength of a weld, with an independent confirmation of the size and volume fractions of the precipitates. In the present approach, one parameter related to the thermal profile in the weld was fitted (q). All other parameters, save one, were taken from an earlier analysis.[16] This one exception is the precipitate/matrix interfacial energy for S phase, which was taken as the average of two temperature dependent functions determined in earlier work. The verification of model predictions in the present and the companion paper,[16] involves independent verification through measurement of precipitate sizes through direct imaging of precipitates (TEM) for treatments in the range 190–400°C, direct measurement of transformation rates over the range 20–500°C (by calorimetry) and hardness/strength data for treatments in the range 150–500°C. Overall, the model performs
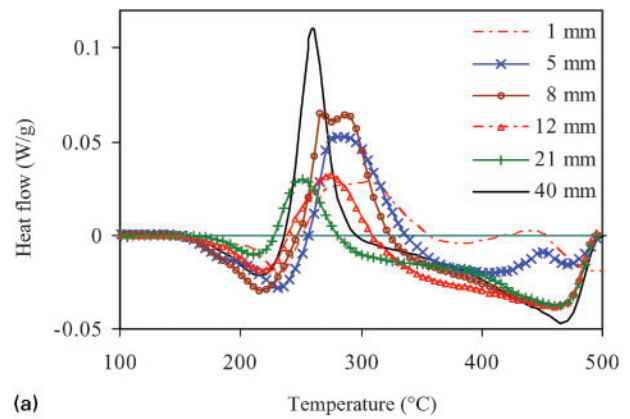
6 *a* **DSC scans obtained from samples extracted at various distances relative to weld, with *b* predicted and measured normalised heat contents of co-cluster dissolution effect**

well, but the work also reveals issues that need further discussion.

It is worthwhile to reiterate that the temperature profile adopted is based on the assumption of zero heat flow in the direction normal to the plate, with constant thermal properties (independent of time and position). This is computationally very efficient, but refinements of this, at computational costs, are certainly possible. Three-dimensional finite element calculations will allow heat flows in the direction normal to the plate to be included, provided the thermal contact between surface of plate and the medium around the plate (possibly air) and possible support of the plate in the form of metal contacts (possibly steel) can be accurately described. It should also be noted that microstructural evolution continually modifies the constitutive material properties and response, in this case, changes in heat conductivity and heat generation within the material can be relevant. In the present alloy, the thermal conductivity at room temperature can vary by 20% depending on the amount of elements dissolved, which is the key factor determining conductivity.[31] The second coupling between models is caused by the heat evolution caused by the reaction in

Table 1 Measured average diameter of S precipitates as obtained from TEM

| Distance from fusion zone, mm	Average radius, nm	Standard deviation, nm	Standard error*, nm	Measured precipitates (no.)
12·5	14·6	4	0·47	72
22·5	6·9	1·81	0·23	64

*Standard error=standard deviation/(N)$^{1/2}$, where N is the number of measured precipitates.

the material. Especially precipitation and dissolution reactions can cause a heat evolution that has a significant impact on the local temperature. For example, the formation of S phase in 2024 Al generates an exothermic heat of 18 J g^{-1}, which equates to a temperature rise of the alloy of about 20 K. Depending on temperature range, such a temperature change can cause a misprediction of strength of upto $\sim$30 MPa[32] or misprediction of hardness of $\sim$10 HV.

Issues surrounding the choice of interfacial energy in KW type models need careful consideration. It should be noted that in relation to interfacial energy, these models are making simplifying assumptions, as local free energy at and near the interface will depend on a range of issues such as local crystallographic orientation of the interface (which changes with heat treatment[18]), vibration energy of the atoms (i.e. causing an entropy term), local misfit strains (which will be temperature dependent) and the possible presence of dislocations relieving interfacial stresses. Thus temperature, ageing time, precipitate size, availability of vacancies and presence of dislocations can all influence local free energy at and near the interface. Thus, it is not surprising that the use of a single interfacial energy for the nucleation and growth stages in the KW leads to erroneous model predictions,[33] and even models assuming either a temperature dependent or a size dependent interface energy[34,35] can only be an approximation.

The precipitate/matrix interfacial energy influences especially the nucleation rate and the coarsening rate. An increase in the interfacial energy value results in lowering the hardness and shifting the transformation reaction (peak of heat flow representing S phase kinetics) to a higher temperature and *vice versa*. Before the authors' papers,[16,28] experimentally measured values for the interfacial energy of the S phase precipitates were not available and in KW type models, it is generally set as a fitting parameter.[36] The values used in this work are within the broad range of values reported for coherent and semicoherent interfaces for θ' precipitates in Al–Cu alloys.[37–41] In the current modelling approach, there is a slight variation for the fitted interfacial energy between the isothermal, and controlled non-isothermal and the present non-isothermal (fusion welding) treatment. While a single temperature dependent formulation applicable to all the three process could not be achieved, the interfacial energy the three treatments are very similar (Fig. 7): differences are less that 2·5%. On the one hand, these small differences point at a good level of consistency in the application of the model among the three types of heat treatment. But it can also be taken as confirmation of the above mentioned limitations of the KW type approach, i.e. assuming that a temperature dependent interface energy is an approximation, and its limitations are revealed when very wide range of heat treatments, such as investigated here, is considered.

The interfacial energy was found to decrease with temperature (Fig. 7). The basic mechanism responsible for this can be understood by noting that at low temperatures for a sharp interface, the interfacial energy can be considered constant, but for in cases where precipitation or dissolution occurs close to the limit of stability of the precipitate, the interface becomes wider and entropy contributions will cause a temperature
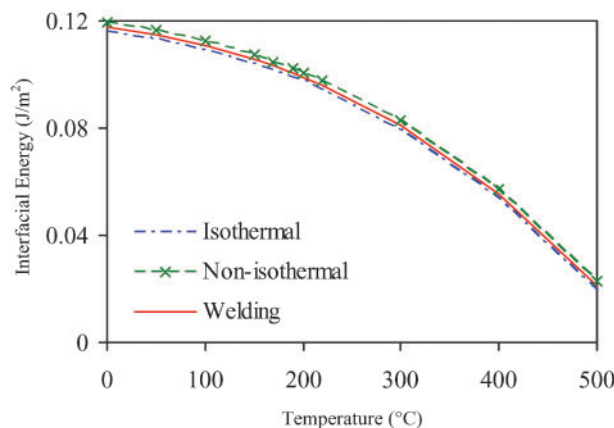
7 Model formulations for precipitate/matrix interface energy for isothermal, non-isothermal (controlled heating/cooling) and non-isothermal (fusion welding) treatments

dependence. This interfacial entropy would cause a decrease of the effective interfacial energy.[42,43]

A further issue in relation to the KW model is that it applies a drastic approximation in describing the three-dimensional distribution of solute around any precipitate by just two parameters: the local concentration in the matrix right next to the precipitate and the average concentration. This approximation implicitly makes a number of assumptions, one of which is that the concentration profile $c(r,t)$ in the section of matrix nearest to one particular precipitate is monotonically decreasing or increasing with r. However, for fast changes in temperature, this assumption can break down, and $c(r,t)$ in the matrix nearest to one particular precipitate may have multiple minima and maxima. Thus the KW model will become progressively more inaccurate as rate of temperature changes increases. In this light, the very small adjustments in interfacial energy ($<$2·5%) between the different groups of heat treatment (with vastly different heating rates) seem limited and indicate that while the (apparent) interfacial energy is slightly adjusted to cope with the KW model becoming progressively more inaccurate as rate of temperature changes increases, the KW model formulation remains a good approximation of average growth rates of precipitates up to the very high heating rates encountered in welding (in excess of 1°C s^{-1}).

Sequence of reactions in Al–Cu–Mg welds

In a recent publication,[18] it was shown that in solution treated Al–Cu–Mg alloys, S phase can precipitate in two forms: type I and type II, causing two overlapping exothermic effects in DSC thermograms in the range 250–330°C, nearly identical to the DSC thermograms of samples at 5, 8 and 12 mm from the weld centre. The higher temperature peak is caused by the formation of type II S phase precipitates which have an orientation relationship that is rotated by $\sim$4° to type I. However, in solution treated and subsequently stretched or cold worked samples, only type I S phase forms. With this detailed work on the formation conditions for variants of S phase being available,[18] and co-cluster formation and dissolution having been studied in some detail,[44] it is possible to offer a full and consistent explanation of reactions occurring during welding and the resultant

nano- and microstructures, as well as the DSC scans of the as welded material in Fig. 6a. This synthesis is as follows. In the 2024 plate at 40 mm from the weld, the temperature reaches ∼200°C (Fig. 1). The temperature–time exposure $T(t)$ seen by the material at this location is too low to see significant S phase formation, as is predicted by the present model and experimentally shown by DSC experiments on 2024-T351 material.[18,45] Co-cluster dissolution will occur during the heating, but this is being followed by co-cluster reformation during the cooling part of the cycle. The substantial amount of dislocations present in the 2024-T351 plate will not be substantially altered. The subsequent DSC run thus reveals heat effects due to substantial co-cluster dissolution and formation of S type I phase on dislocations. Formation of S type II phase is suppressed due to the extensive formation of S type I phase. In the 2024 plate at 21 mm from the weld, the temperature reaches ∼275°C (Fig. 1). The temperature–time exposure $T(t)$ experienced by the material at this location will cause significant S phase formation, as is predicted by the present model, and the availability of dislocations will cause the S phase to form as the type I variant. S phase formation is not complete and hence the DSC curve shows effects due to some co-cluster dissolution and some further S phase (type I) formation mainly due to growth of pre-exiting precipitates. The latter explains why the S phase formation effect shows a small shift to lower temperature. At about 12–8 mm from the weld centre, substantial amounts of S phase have formed during the temperature–time exposure $T(t)$ experienced by the material and dislocations have been annealed out, while some limited co-cluster reformation has occurred during the cooling part. The DSC curves then show co-cluster dissolution (this may be called redissolution), and the absence of dislocations will slow the formation of type I S phase, allowing significant type II S phase formation. The formation of these two types of S phase causes the double peak appearance in the corresponding DSC scan between 250 and 310°C (Fig. 6a). In the 2024 plate at 5 mm from the weld, the temperature reaches ∼600°C (Fig 1). The material at this location will have seen dissolution of all precipitates followed by partial melting, and during cooling and the subsequent storage period, substantial co-cluster reformation will have occurred. The DSC scan then shows co-cluster dissolution (this may be called redissolution), and the absence of dislocations will slow the formation of type I S phase, allowing significant type II S phase formation. At this location, solute 'loss' to eutectic phases is limited and hence dissolution and precipitation effects in the scan are strong. Finally, at 1 mm from the weld centreline, the material will have seen temperatures well in excess of 650°C, leading to full melting. The DSC scan then shows co-cluster redissolution, and the absence of dislocations will allow formation of both type I and type II S phase (Fig. 6a). In this resolidified material, solute 'loss' to eutectic phases is substantial and the heat effects will be smaller than those in the material at 5 mm from the weld, which was partially melted.

Following the analysis in the previous paragraph, it is clear that modelling of precipitation reactions and strength in welds of the present cold worked alloys can be further refined by considering local evolution of dislocation densities and its influences on the formation of precipitates that form on these dislocations (in this case, the type I S phase). In a semiquantitative manner, it can be expected that inclusion of these issues would modify the model to predict somewhat slower S phase formation during cooling after heating to temperatures beyond the recovery stage. This can explain the underprediction of hardness by the present model at and ∼12 mm from the weld centre (Fig. 2), where formation and growth of coarse S phase, which reduces subsequent co-cluster reformation, influences the strength prediction. This explanation is supported by the difference between amounts of co-clusters predicted and measured at this location (Fig. 6b). However, it should be noted that details of the interaction between S phase formation and dislocations will in most areas of the weld be of very limited importance for predictions of local strength.

Feasibility of post-welding treatments

In agreement with qualitative and semiquantitative interpretations made in literature, the present work, through a quantitative model, shows that parts of the weld will permanently be weaker than solution treated and aged alloys because alloying elements are incorporated either in coarsened precipitate phases (in 2024, this is predominantly S phase) and/or in eutectic phases, where they become largely ineffective in strengthening. And they would also adversely affect properties such as toughness, fatigue resistance and corrosion resistance. Only post-welding solution heat treatment can release these elements and make them available for precipitation hardening, but solution heat treatment is generally not possible for welded assemblies. The above discussion relating to types I and II S phase reveals one further issue related to the practice of post-welding ageing. While the present results show that certain areas of the weld will respond to a post-welding heat treatment through conversion of co-clusters to S phase, it is not possible to obtain the same relative amounts of types I and II S phase that would be obtained by direct heat treatment of Al–Cu–Mg solution heat treated and stretched material (for instance, 2024-T351), because the annihilation of dislocations will suppress type I S phase and generally slows down the formation of S phase (necessitating a high ageing temperature for S phase formation). This indicates that even the small areas that have seen substantive resolutionising cannot be heat treated to obtain full conversion of available Cu to the beneficial type I S phase in post-welding ageing.

Importance of co-clusters

An important finding of the present work is the crucial importance of the co-clusters in determining the local strength and hardness of the weld. The model for co-cluster strengthening adopted here has been derived by one of the authors with co-workers[30,46] through analyses that involved three-dimensional atom probe analysis, DSC, isothermal calorimetry and mechanical tests of a range of Al–Cu–Mg alloys. Hence this part of the model is thought to have a good physical basis. However, refining this model by including chemical strengthening contributions may well be possible. The co-clusters can range in size from just a few atoms (essentially a subnanometre scale cluster)[30,44] to hundreds of atoms. In regions of the weld where strengthening due to S phase is low or totally absent, e.g. in the fusion zone and around the minimum in hardness at about 10–13 mm

from the centre, it is the co-clusters that provide typically 70–80% of the resistance to dislocation movement. It is these regions that will fail on loading normal to the weld, and hence it is the co-clusters that are nearly exclusively responsible for the strength of Al–Cu–Mg welds.

Conclusion

A new model has been applied to predict the microstructural and strengthening changes in Al–Cu–Mg alloys during fusion welding. The solid state part of the model has previously been developed and tested for isothermal and controlled heating/cooling treatments by the authors, and the parameters, with exception of those used for determining the interface energy, are the same in all the three model formulations, i.e. isothermal, controlled heating/cooling and fusion welding. The precipitation strengthening in Al–Cu–Mg alloys, with Cu/Mg ratio close to 1, is due to the shearable Cu–Mg co-clusters and the non-shearable S phase precipitates. The model predictions and the experimental results are in good agreement. The co-clusters are identified as the main strengthening (pre-)precipitates responsible for the strength of Al–Cu–Mg welds.

Acknowledgements

References

1. E. A. Starke and J. T. Staley: *Prog. Aerosp. Sci.*, 1996, **32**, 131.
2. M. B. Prime, T. Gnaupel-Herold, J. A. Baumann, R. J. Lederich, D. M. Bowden and R. J. Sebring: *Acta Mater.*, 2006, **54**, 4013.
3. C. Genevois, A. Deschamps, A. Denquin and B. Doisneau-Cottignies: *Acta Mater.*, 2005, **53**, 2447.
4. C. Zhou, X. Yang and G. Luan: *Mater. Sci. Eng. A*, 2006, **A418**, 155.
5. N. Kamp, N. Gao N, M. J. Starink and I. Sinclair: *Int. J. Fatigue*, 2007, **29**, 869.
6. M. R. Urban: *Int. J. Fatigue*, 2003, **25**, 1013.
7. B. Langrand, L. Patronelli, E. Deletombe, E. Markiewicz and P. Drazetic: *Aerosp. Sci. Technol.*, 2002, **6**, 333.
8. A. Heinz, A. Haszler, C. Keidel, S. Moldenhauer and W. S. Miller: *Mater. Sci. Eng. A*, 2000, **A280**, 102.
9. F. Lefebvre, F. Ganguly and I. Sinclair: *Mater. Sci. Eng. A*, 2005, **A397**, 338.
10. R. V. Preston, H. R. Shercliff, P. J. Withers and S. Smith: *Acta Mater.*, 2004, **52**, 4973.
11. Z. Liu, Q. Wang and B. Zheng: *J. Mater. Process. Technol.* 2001, **115**, 373.
12. E. Saad, H. Wang and R. Kovacevic: *J. Mater. Process. Technol.*, 2006, **174**, 127.
13. S. M. Aithala and V. V. Subramaniam: *J. Appl. Phys.*, 1998, **84**, 3508.
14. H. X. Wang, Y. H. Wei and C. L. Yang: *Compos. Mater. Sci.*, 2007, **38**, 571.
15. A. Urena, E. Otero, M. V. Utrilla and C. J. Munez: *J. Mater. Process. Technol.*, 2007, **182**, 624.
16. I. N. Khan and M. J. Starink: *Mater. Sci. Tech. A*, 2008, Part 1 to this paper, 2008, **24**.
17. Y. A. Chang, S. L. Chen, F. Zhang, X. Yan, F. Xie, R. Schmid-Fetzer and W. A. Oates: *Prog. Mater. Sci.*, 2004, **49**, 313.
18. S. C. Wang and M. J. Starink: *Acta Mater.*, 2007, **55**, 933.
19. O. Grong: 'Metallurgical modeling of welding', 2nd edn; 1997, London, The Institute of Materials.
20. S. A. David, S. S. Babu and J. M. Vitek: *JOM*, 2003, **55**, 14.
21. E. Scheil: *Z. Metallkd*, 1942, **34**, 70.
22. H. S. Carslaw and J. C. Jaeger: 'Conduction of heat in solids', 2nd edn, 266–270; 1959, London, Clarendon Press.
23. S. C. Wang, F. Lefebvre, J. L. Yan, I. Sinclair and M. J. Starink: *Mater. Sci. Eng. A*, 2006, **A431**, 123.
24. A. Belhadja, P. Baudouin, Y. Houbaert: *J. Magn. Magn. Mater.*, 2002, **248**, 34.
25. D. Dye, O. Hunziker and R. C. Reed: *Acta Mater.*, 2001, **49**, 683.
26. J. R. Davis (ed.): 'ASM specialty handbook: aluminum and aluminum alloys'; 1993, Materials Park, OH, ASM International.
27. F. Lefebvre, S. C. Wang, M. J. Starink and I. Sinclair: *Mater. Sci. Forum*, 2002, **396–402**, 1555.
28. I. N. Khan, M. J. Starink and J. L. Yan: *Mater. Sci. Eng. A*, 2008, **472**, 66–74.
29. D. P. P. Booth, M. J. Starink and I. Sinclair: *Mater. Sci. Technol.*, 2007, **23**, 276.
30. M. J. Starink, N. Gao, L. Davin, J. Yan and A. Cerezo: *Philos. Mag.*, 2005, **85**, 1395.
31. M. J. Starink and X. M. Li: *Metall. Mater. Trans. A*, 2003, **34**, 899.
32. M. J. Starink, A. Deschamps and S. C. Wang: *Scr. Mater.*, 2008, **58**, 377–382.
33. J. D. Robson, M. J. Jones and P. B. Prangnell: *Acta Mater.*, 2003, **51**, 1453.
34. C. Sigli: *Mater. Sci. Forum*, 2006, **519–521**, 321.
35. J. C. Werenskiold, A. Deschamps and Y. Brechet: *Mater. Sci. Eng. A*, 2000, **A293**, 267.
36. J. D. Robson and P. B. Prangnell: *Mater. Sci. Eng. A*, 2003, **A352**, 240.
37. J. D. Boyd and R. B. Nicholson: *Acta Metall.*, 1971, **19**, 1101.
38. J. D. Boyd and R. B. Nicholson: *Acta Metall.*, 1971, **19**, 1379.
39. H. I. Aaronson and C. Laird: Ford Motor Co. Scientific Laboratory Report, Ford Motor Co. Scientific Research Laboratory, Dearborn, MI, USA, 1967.
40. C. Wolverton and Z. Ozolins: *Phys. Rev. Lett.*, 2001, **86**, 5518.
41. V. Vaithyanathan, C. Wolverton and L. Q. Chen: *Phys. Rev. Lett.*, 2002, **88**, 125503.
42. Z. G. Yang, T. J. Wang, S. Zhong, G. Yang and G. C. Wang: *J. Mater. Sci.*, 2005, **40**, 701.
43. C. Borchers and R. Bormann: *Acta Mater.*, 2005, **53**, 3695–3701.
44. M. J. Starink, A. Cerezo, J. Yan and N. Gao: *Philos. Mag. Lett.*, 2006, **86**, 243.
45. S. C. Wang, M. J. Starink and N. Gao: *Scr. Mater.*, 2006, **54**, 287.
46. M. J. Starink, P. Wang, I. Sinclair and P. J. Gregson: *Acta Mater.*, 1999, **47**, 3855.